



Shock wave attenuation using rigid obstacles with large- and small-scale geometrical features

Alexander Ivanov¹ · Nicolas Fassardi¹ · Christina Scafidi² · Tal Shemen² · Veronica Eliasson² 

Received: 1 May 2019 / Accepted: 19 June 2019
© Springer Nature Switzerland AG 2019

Abstract

Explosions and their resulting shock waves may pose a large threat to both humans and structures alike. The previous research concludes that a logarithmic spiral configuration is effective in focusing shock waves to a focal point. This research outlines shock tube experiments conducted on two types of solid rectangular obstacles placed in a logarithmic spiral shape. The obstacles have a square cross-sectional area, with one set of obstacles being normal square shapes, but the other set of obstacles have three grooves cut out on every side of the obstacle, thus reducing the cross-section area by 10%. High-speed schlieren photography is used to visualize the shock waves and numerical simulations provide supporting data. A comparison in regards to shock wave attenuation between the two obstacle sets is presented. Results conclude that the three-groove obstacle geometry was successful in attenuating the peak pressure and pressure impulse of a reflected shock wave; however, the results for the transmitted shock wave between the two configurations are again inconclusive.

Keywords Shock dynamics · Shock wave attenuation · Schlieren photography

1 Introduction

Attenuation of shock waves is of importance for many practical applications, such as blast wave propagation through tunnels, unintentional industrial accidents, and high-speed aerospace structural mechanics. For example, by dampening the harmful effects that result from a shock wave, one might

be able to reduce the number of possible injuries or fatalities in any given event. Different types of mitigation techniques using liquids or solid structures have been researched by numerous research groups (Shi and Yamamura 2004; Britan et al. 2006; Seeraj and Skews 2009) with more methods covered in greater detail in the review paper by Igra et al. (2013).

In some scenarios, solid obstacles may provide a cost-effective and easy-to-implement attenuation solution. Solid obstacles allow for passive protection of people and structures without the need for expensive integrated technology. These solid obstacles can either amplify or attenuate the shock wave effects depending on their configuration and the direction of the shock wave.

More recently, technological advancements have made the study of shock wave attenuation more appealing and accessible due to the increased probability of shock wave generation in laboratory and industrial settings. As a result, there has been an increase in need for shock wave attenuation technology and research on physical obstacles to mitigate shock waves. Research has been conducted in the aforementioned subject matter, for example: Igra et al. (2001) used a bent duct geometry, Britan et al. (2006) and Andreopoulos et al. (2007) used porous barriers and grid structures, while Berger et al. (2010) used multiple wall-like barriers. In every case,

This study was supported by the National Science Foundation (NSF) under grant No. CBET-1437412.

✉ Veronica Eliasson
eliasson@ucsd.edu

Alexander Ivanov
alivanov@ucsd.edu

Nicolas Fassardi
nfassard@ucsd.edu

Christina Scafidi
cscafidi@ucsd.edu

Tal Shemen
tshemen@ucsd.edu

¹ Department of Mechanical and Aerospace Engineering, University of California, La Jolla, San Diego, CA 92093-0085, USA

² Department of Structural Engineering, University of California, La Jolla, San Diego, CA 92093-0085, USA

the results showed that placing a physical barrier in the flow led to the attenuation of the shock wave. Following these discoveries, Chaudhuri et al. (2013) conducted numerical analysis on a variety of obstacles placed in grid-like formations. These obstacles were comprised of geometries with various cross-sections including circles, rectangles, and triangles. Expanding beyond obstacles in a grid pattern Wan and Eliasson (2015) also used solid obstacles, but configured them into the shape of a logarithmic spiral. The logarithmic spiral shape was chosen based on the previous work by Milton and Archer (1969) in which a solid logarithmic spiral converging duct showed that all of the shock wave was propagated towards the focal point without loss of energy through reflections off the side walls. Wan and Eliasson concluded that solid obstacles oriented in the shape of a logarithmic spiral allowed for attenuation due to its ability to slow the formation of a transmitted shock wave. In that same year, Berger et al. (2015) continued to explore shock wave attenuation using numerical simulations based on obstacle formations used by Berger et al. (2010) but with single barriers. Vortex shedding was investigated, and the study concluded that vortex shedding off the edges of obstacles played a significant role in attenuating the strength of the transmitted shock waves.

The current experimental study on logarithmic spirals has focused on whether vortex shedding plays a significant role in reducing the strength of both the transmitted and reflected shock waves. This work compares the results from groove and non-groove obstacles placed in a logarithmic spiral pattern mainly through experimentation and investigates the configuration's ability to promote vortex shedding and its ability to attenuate shock waves. One might ask if the large-scale geometry, i.e., the logarithmic spiral pattern in which obstacles are placed, is more important than the small-scale geometry, i.e., the grooves that were cut on the surface of each obstacle. The previous work by Wan and Eliasson (2015) looked into the large-scale geometrical effects by comparing obstacles placed in a logarithmic spiral shape with obstacles placed in various other patterns. This current study compares attenuation effects due to small-scale features of the obstacles. To define shock wave attenuation in this study, both transmitted and reflected shock waves were considered.

Often times reflected shock waves can be just as dangerous, if not more dangerous than a transmitted shock wave. This is because a reflected shock wave propagates back upstream and can produce even higher temperatures and pressures than the incident shock wave. Transmitted and reflected shock wave attenuation will be characterized through numerical factors which include changes in pressure impulse and peak pressure. Evaluating these different criteria for both the reflected and transmitted shock waves will be used to judge whether the shock waves have been attenuated, and by how large a degree attenuation was obtained.

2 Experimental setup

Experiments were conducted using a horizontally mounted shock tube with obstacles placed in a logarithmic spiral pattern inside the shock tube test section. High-speed schlieren visualizations were utilized together with local pressure measurements taken at several locations on the shock tube, both upstream and downstream of the test section.

2.1 Shock tube

The horizontal shock tube, shown in Fig. 1, consists of a driver section, a driven section, and a test section that contains the obstacles. The driver and driven section are separated using a moisture-resistant polyester membrane, also referred to as a mylar membrane. Membrane thickness is chosen so as to allow for the desired Mach number of the shock wave to be produced. The driver section is fastened to the driven section using four sets of nuts, bolts, and spacers around the perimeter of the joined faces of the sections. Both the driven section and the test section have square inner cross-sections of the same dimensions. The driven section was designed to be long enough to allow the compressive waves produced by the rupture of the mylar membrane to coalesce into a planar shock wave before reaching the test section. The test section is attached to the end of the driven section and left open to the surrounding laboratory environment. The test section is equipped with clear acrylic viewing windows that are aligned with the z -folded schlieren optical system to allow the high-

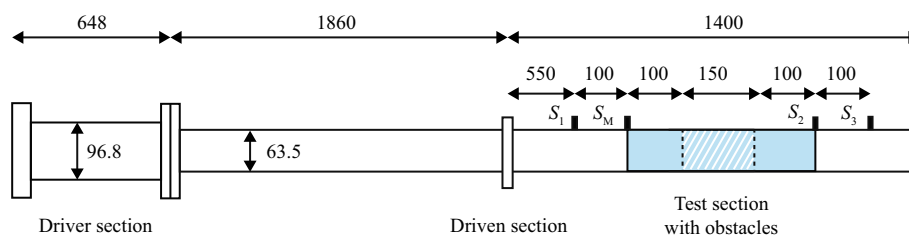


Fig. 1 (Color online) Full shock tube consisting of a driver section, driven section, and test section, all made of aluminum. The light blue section in the test section represents the clear acrylic windows, and the lined pattern indicates the location of the obstacles. Dimensions in mm, not to scale

speed camera (Shimadzu HPV-X2) to gather experimental shock wave footage.

2.2 Pressure measurements

To develop a shock wave Mach number of 1.20 in the test section of the shock tube, a significant pressure differential between the driver section and ambient pressure needs to exist, since the test section is at atmospheric conditions through its open end. Using a compressed air tank, the driver section is pressurized to 138 ± 0.7 kPa (measured using a Druck DPI 104 Pressure Testing Gauge with 0.05% full-scale accuracy) corresponding to the desired Mach 1.20 incident shock wave. To release the driver gas to the downstream driven section, the mylar membrane is ruptured using an arrowhead that pierces the membrane at the desired pressure differential. The arrowhead is held back using an electromagnet until it is disengaged to pierce the mylar membrane.

To ensure that the membrane was pierced as expected and that the intended shock Mach number was achieved, the time of arrival was measured between two pressure sensors located upstream of the obstacle section (sensors S_1 and S_M in Fig. 1). All data used for analysis in this study fell within 2% of the intended Mach number of 1.20.

Shock wave data are gathered using four pressure sensors (Piezoelectronic Model #113B21) placed upstream and downstream of the test section. The sensors that are used to collect pressure data are noted as $S_1 - S_3$ respectively, where S_1 is the sensor closest to the driver section. The pressure sensor placed upstream of the test section, S_1 , measures both the incident and reflected shock waves. Downstream of the test section, pressure sensors S_2 and S_3 measure the transmitted shock wave. Pressure sensor S_M is used only to obtain the shock Mach number of the incident shock wave. As the shock wave passes through the shock tube, the pressure signals from the sensors are relayed to a signal conditioner (PCB Signal Generator—482C05) and then read by an oscilloscope (Picoscope 4824). The oscilloscope has a resolution of ± 500 mV and the voltage is then converted to pressure using the corresponding sensitivity for each pressure sensor provided by the PCB calibration data (S_1 : 3.646 mV/kPa, S_2 : 3.590 mV/kPa, and S_3 : 3.722 mV/kPa).

The pressure sensors were strategically placed to allow for the shock wave Mach number to be measured using the distance between sensors and the elapsed time. The shock wave passing over a pressure sensor produces a distinct jump in pressure that the oscilloscope records. The elapsed time of the shock wave passing the sensors is calculated using these abrupt changes in pressure, and thus, the incident shock wave Mach number can be calculated using the following:

$$M_s = \frac{\Delta x / \Delta t}{\sqrt{\gamma R(T + 273.15)}}, \quad (1)$$

where Δx is the known distance between pressure sensors, Δt is the time elapsed, γ is the specific heat ratio for the driven gas, R is the specific gas constant for the driven gas, and T is the ambient temperature in degrees Kelvin, with the assumptions: $\gamma = 1.4$ and $R = 287$ J/(kg · K). At the beginning of each experiment, the ambient temperature and pressure in the room are recorded. These values are taken into account when calculating the speed of sound for each experiment.

2.3 Test section

Two different obstacle geometries are considered: one spiral has a square cross-section, also referred to as a zero-groove obstacle, and the other has three semi-circular grooves cut out from each side of the obstacle, as illustrated in Fig. 2. Each groove has a radius of 0.52 mm and collectively the cut out material corresponds to 10% of the total side-cross-sectional area of the obstacle.

The two kinds of obstacles are then placed in a logarithmic spiral pattern, each consisting of 15 obstacles, inside the test section of the shock tube (Fig. 3). The placements follow that outlined in the numerical simulations described in Wan and Eliasson (2015). The sides of the test section are made of clear acrylic windows of the same thickness as the rest of the shock tube test section and aluminum base plates that mount into the test section of the shock tube. The ends of each aluminum obstacle have two 2 mm-diameter grounding

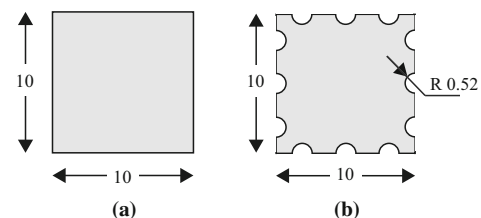


Fig. 2 Zero- and three-groove obstacles side-by-side comparison. Dimensions in mm, not to scale

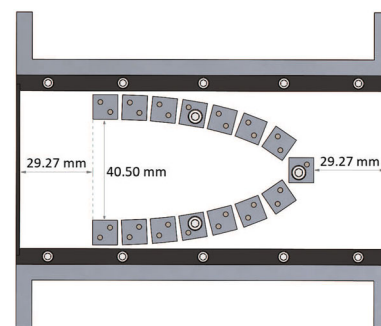
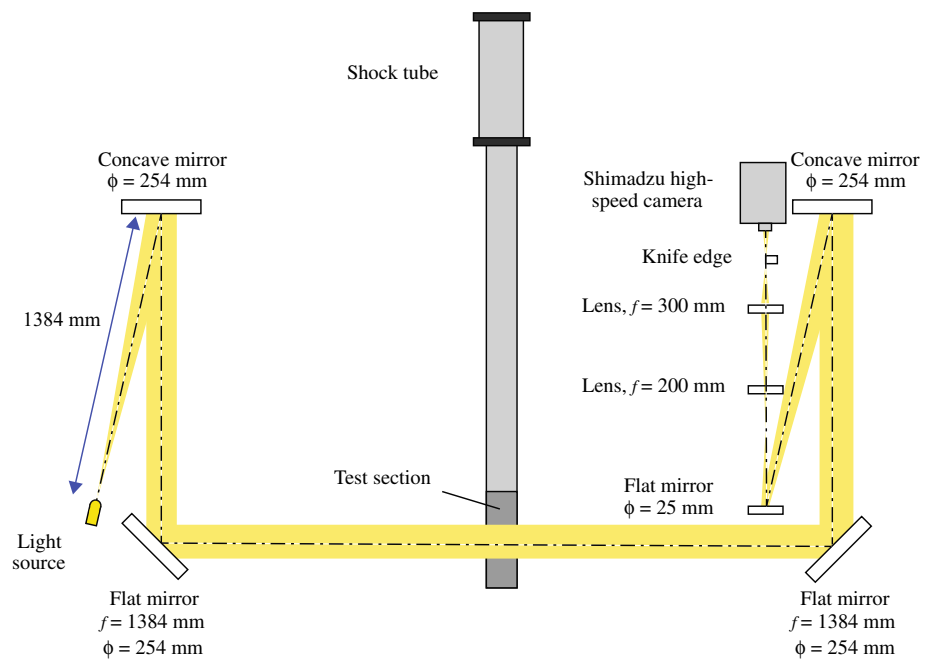


Fig. 3 (Color online) Two-dimensional side view of the zero-groove logarithmic obstacles that are placed within test section of the shock tube

Fig. 4 (Color online) Schlieren setup with f representing the focal length of the lens or mirror and Φ being the diameter of the lens or the mirror



pins that prevent rotation of the obstacles as the shock wave passes through the test section. Three of the fifteen obstacles have a screw instead of the pin to keep the test section walls parallel as the shock passes through. In addition, between each pin and obstacle, there is a rubber gasket to keep the test section airtight during the experiment. Along the lengths of the acrylic panels and between the aluminum base plates, additional rubber gasket is placed to keep the test section airtight. Both the zero- and three-groove obstacles are placed in the same logarithmic spiral orientation.

2.4 Schlieren setup

A z-folded schlieren setup (Fig. 4) is used to capture schlieren photographs of the shock dynamic events as the shock wave passes through the test section of the shock tube. A concave mirror is used to collimate light from the light source as it passes through the test section. After the light passes through the test section, another concave mirror is used to re-focus the light onto a series of lenses into the Shimadzu high-speed camera. The clear acrylic windows in the shock tube test section allow the collimated light from the z-folded schlieren setup to pass through the zone of interest and into the high-speed camera. The high-speed camera is set to record at variable frame rates depending on the experimental case being investigated.

3 Experimental procedure

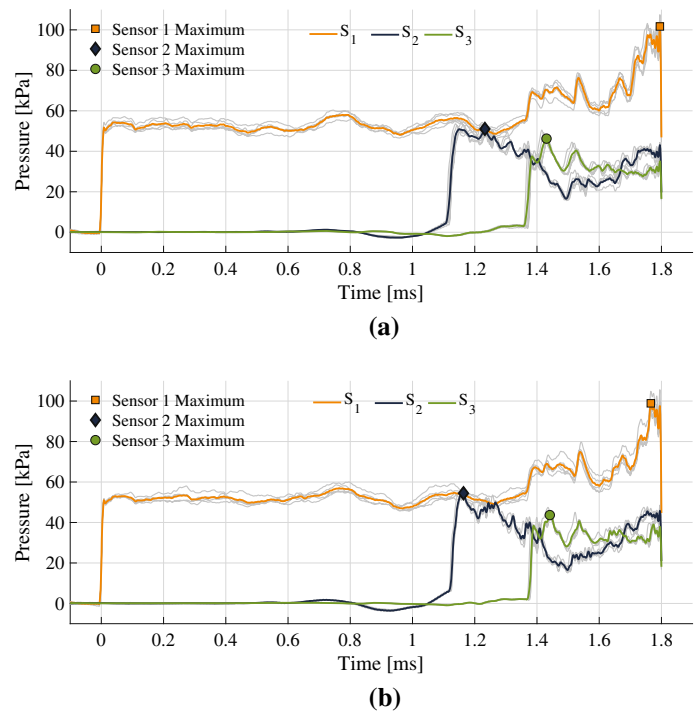
Initially, the connections throughout the shock tube, such as the joining of the driver and driven sections, need to be eval-

uated to ensure they are airtight. Afterwards, pressure sensor connections must be checked, and the high-speed camera must be configured to record once the shock wave passes sensor S_1 . Next, a mylar membrane is placed between the driver and driven sections. Here, a $25.4 \mu\text{m}$ -thick mylar membrane is used to produce a Mach 1.20 shock wave. The driver and driven sections are fastened together and the driven section is pressurized. Compressed air gradually fills the driver section at a rate of approximately 0.05 kPa/s to mitigate the risk of early membrane rupture. Complete pressurization of the driver section takes approximately 7 min for these experiments. Once the pressure level in the driver section stabilizes to $20 \pm 0.10 \text{ kPa}$, the membrane is ruptured by disengaging the electromagnet that releases the arrowhead, such that it punctures the mylar membrane. For the experiment to be considered valid, the properties of the incident planar shock wave must be evaluated. An experiment is only considered valid if the incident planar shock wave velocity is within 2% of the design case of Mach 1.20. Once the experiment is complete, the driver and driven sections are separated and the mylar membrane is replaced with a new membrane. Experiments were repeated until five experiments that fit the design criteria were obtained.

4 Results

The results from the experimentation will focus on the pressures measured by the most upstream and most downstream sensors, S_1 and S_3 . It should be noted that the incident shock wave is planar, and thus, the upstream pressure sensor, S_1 , records the actual shock strength until the reflected waves

Fig. 5 (Color online) Pressure measured from sensors S_1 , S_2 , and S_3 each case is repeated five times. Each experiment is marked in grey, and the average result from each sensor is marked in color. The maximum pressure is marked by a filled symbol. **(a)** Zero-groove setup; **(b)** three-groove setup



arrive. At that time, the shock strength varies across the shock surface. The downstream pressure sensor, S_3 , also measures a local shock strength value, because, downstream of the obstacles, the shock wave strength also varies across the shock surface. However, since the initial shock Mach number is fairly low ($M_s = 1.20$), the shock strength variation along the shock front is limited.

After analyzing visual and numerical results from both pressure sensors, different conclusions were met regarding the mitigation of the reflected and transmitted shock waves. Throughout the experimentation, five sets of data were obtained from both the zero-groove logarithmic spiral and the three-groove logarithmic spiral, as shown in Fig. 5. When analyzing the reflected shock wave data, which corresponds to the pressure recorded by sensor S_1 , the three-groove logarithmic spiral resulted in lower than average peak pressure and pressure-impulse results than its zero-groove counterpart. While the three-groove logarithmic spiral outperformed the zero-groove counterpart in mitigating the reflected shock wave, the results for the transmitted shock wave were less definitive.

4.1 Shock wave attenuation

When looking at the experimental results from both cases, it is important to clearly define an attenuation factor; the attenuation factor will serve as a standard by which the successes and failures of the experiments can be objectively measured. For the attenuation of shock waves, it was determined that there are two primary factors which must be taken in consid-

eration equally, namely: peak pressure and pressure impulse. Peak pressure is defined as maximum pressure experienced by a pressure sensor throughout the testing time interval after the shock wave initially interacts with sensor S_1 . Pressure impulse is defined as $\int_{t_0}^{t_f} P dt$, where t_0 is the time that the shock wave first reaches the sensor and t_f is the length of the testing time, and here, $t_f = 1.8$ ms.

4.2 Experiment replicability

In both the zero- and three-groove cases, five experiments were performed to gather pressure sensor data, as shown in Fig. 5. In this study, for the experiment to be considered valid, the incident planar shock wave Mach number needed to be within 2% of the ideal experimental value of Mach 1.20. All five experiments fulfill this criteria for both zero- and three-groove experiments, as shown in Fig. 5a, b. The average of these five experiments was then plotted over the five individual experiments. The five individual experiments are represented in grey and the average is the colored lines. For both experimental cases, the average follows the same trend of the individual experiments. This information confirms that the experiment and results can be replicated with high repeatability. The numerical results are presented in Tables 1 and 2. The numerical comparison between the two different setups, zero-groove and three-groove, will be done using the average of the five experiments from each experimental setup.

The success rate of an experiment, for an experiment's incident shock wave to be within 2% of the design case of

Table 1 Peak pressure measured by each sensor for the five repeated experiments for the zero-groove logarithmic spiral case

	Peak pressure [kPa]		
	Sensor S_1	Sensor S_2	Sensor S_3
Experiment 1	96.97	51.21	46.54
Experiment 2	102.53	50.84	47.33
Experiment 3	104.41	53.05	49.09
Experiment 4	107.50	54.38	50.49
Experiment 5	96.92	51.89	47.96
Average	101.67	52.27	48.28
Std. Dev.	4.66	1.45	1.55

Table 2 Peak pressure measured by each sensor for the five repeated experiments for the three-groove logarithmic spiral case

	Peak pressure [kPa]		
	Sensor S_1	Sensor S_2	Sensor S_3
Experiment 1	97.27	53.51	43.33
Experiment 2	95.28	54.57	42.84
Experiment 3	105.62	57.02	47.45
Experiment 4	100.03	55.74	44.45
Experiment 5	98.15	55.25	44.27
Average	99.27	55.22	44.47
Std. Dev.	3.94	1.31	1.80

Mach 1.20, was 83%, where the average Mach number of the zero- and three-groove experiments was 1.189 and 1.187 respectively. Only those experiments that fell within the 2% of the design Mach number were used to analyze the data in this study.

4.3 Single obstacle experiments

To investigate the interactions between shock waves and the different small-scale geometries on the obstacles themselves, single obstacle experiments were conducted and then compared to numerical simulations. The zero-groove and three-groove obstacle results are shown in Figs. 6 and 7, respectively. The simulations were performed using Overture, an object-oriented code framework for solving partial differential equations on overlapping grids (Henshaw and Schwendeman 2003, 2006). The numerical simulations replicated the experiment in which a Mach 1.20 planar shock wave interacts with a single zero- or a single three-groove obstacle, respectively. The simulations were performed by solving the Euler equations of gas dynamics using an ideal equation of state. The initial conditions were such that the Mach 1.20 shock wave propagated into the standard atmospheric conditions at room temperature. Details of the equations, initial conditions, and the solver itself are further

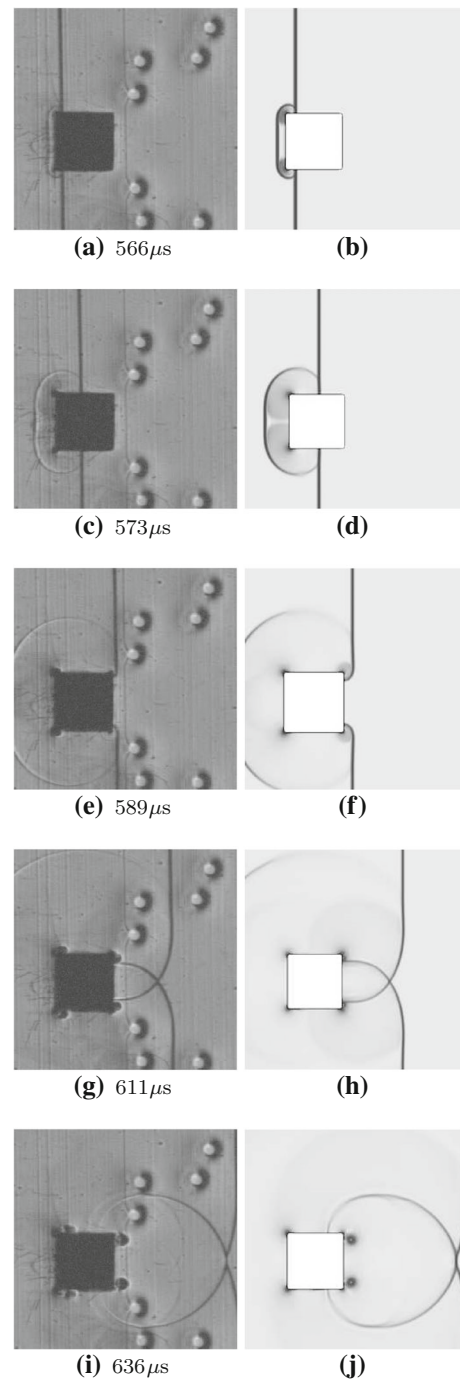


Fig. 6 Experimental schlieren photographs in the left column and numerical simulation schlieren images in the right column for the case of a single zero-groove obstacle in the test section. Time 0 μ s corresponds to the time instant when the shock wave passes sensor S_1

described in prior work (Wan and Eliasson 2015). The single obstacle experiments were setup using the same test section that is used for the full logarithmic spiral while keeping only the center obstacle and removing all other obstacles. Thus, the dark circles present in the photographs of Figs. 6 and

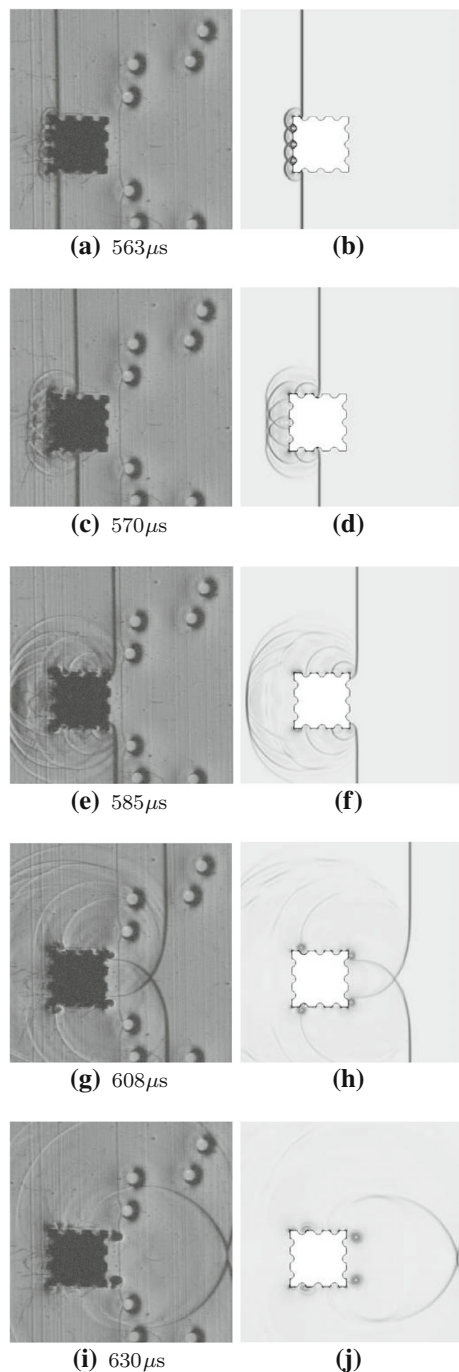


Fig. 7 Experimental schlieren photographs in the left column and numerical simulation schlieren images in the right column for the case of a single three-groove obstacle in the test section. Time $0 \mu\text{s}$ corresponds to the time instant when the shock wave passes sensor S_1

7 are the holes in the test section windows where the other obstacles usually bolt in place.

For both the experiments, the high-speed camera was triggered when the shock wave passed over sensor S_1 , but the recording was delayed appropriately to capture the shock wave as it passed the obstacle. When comparing the exper-

imental schlieren images with the numerical simulation results, it is clear that the simulations very closely resemble the experimental results. When comparing Figs. 6 and 7, differences between the two obstacles become apparent. As the shock wave propagates over the zero- and three-groove obstacles, reflected shock waves form. Both the experiments and the simulations show that the three-groove obstacles produce more reflected shock waves. Another phenomenon that has been observed can be seen in Fig. 7, whereas the shock wave propagates over the three-groove obstacle and small vortices form within the grooves of the obstacle. Furthermore, in frames (g)–(j) of both Figs. 6 and 7, vortices can be seen separating from the surface of the obstacles. To investigate why the three-groove obstacles were able to better mitigate the shock waves than their zero-groove counterparts, the simulation results were used to investigate the vorticity production in the flow. Figure 8 shows the vorticity at three time instants for both types of obstacle. The vortex shedding along the incident edge of the obstacle is more significant in the three-groove case. In addition, the trailing edge vortices that shed off of the body of the three-groove obstacle are also visibly larger than for the zero-groove obstacle counterpart.

The single obstacle experiments and simulations exemplified the appealing characteristics of the three-groove obstacle. By themselves, the obstacles were able to generate more vorticity and reflected shock waves, ultimately contributing to the mitigation of the reflected and transmitted shock waves.

4.4 Logarithmic spiral visual analysis

Schlieren photographs for the zero- and three-groove logarithmic spirals are shown in Figs. 9 and 10, respectively. The schlieren photographs show that more reflected shock waves are produced when the planar shock wave makes contact with the three-groove logarithmic spiral, i.e., compare Figs. 9c, and 10c. This follows the same trend throughout the entirety of the shock passing through the rest of the logarithmic spiral, and is in accordance to what was observed in the single obstacle experiments. The gap between the obstacles allows the shock wave to turn perpendicular to its initial direction and interact with the top and bottom of the shock tube. That shock wave is forced to once again turn 90° and forms another shock wave that propagates between the shock tube walls and the outside of the obstacles. This shock wave trails behind the incident shock, which is clearly shown in Figs. 9c and 10c. Vortex formation around each obstacle is also produced, and in particular, the vortices near the entrance to the logarithmic spiral are observed. These vortices were also observed in the previous work by Wan and Eliasson (2015).

As the shock wave continues to propagate through the logarithmic spiral, the size of the incident planar shock wave is

Fig. 8 Numerical simulations showing vorticity plots for early time (left) to late time (right) for a single obstacle with zero grooves (top row) and three grooves (bottom row). The respective frames for the zero- and three-groove obstacles are taken at the same simulation time

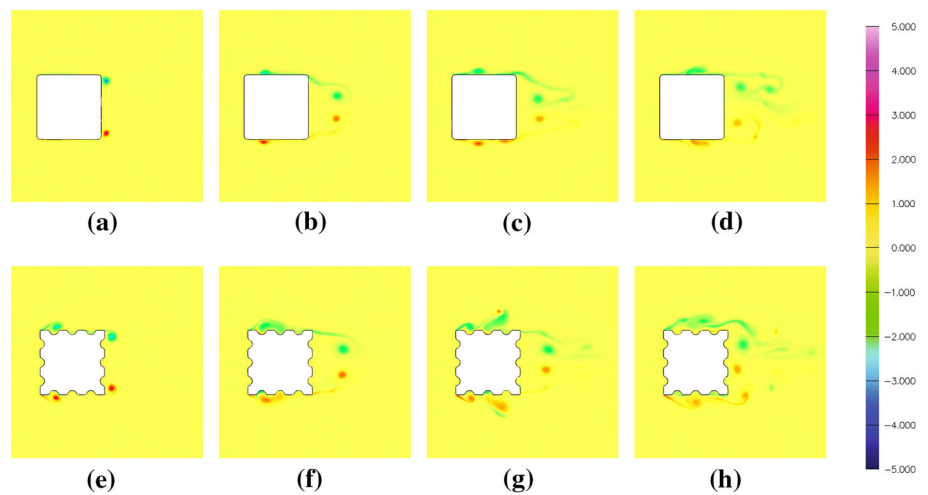


Fig. 9 Experimental schlieren photographs for the case of a logarithmic spiral with zero-groove obstacles. Time $t = 0 \mu\text{s}$ corresponds to the time instant when the shock wave passes sensor S_1 . The arrow in frame (e) shows the location of the reflected shock wave. Frame rate: 250,000 frames per second

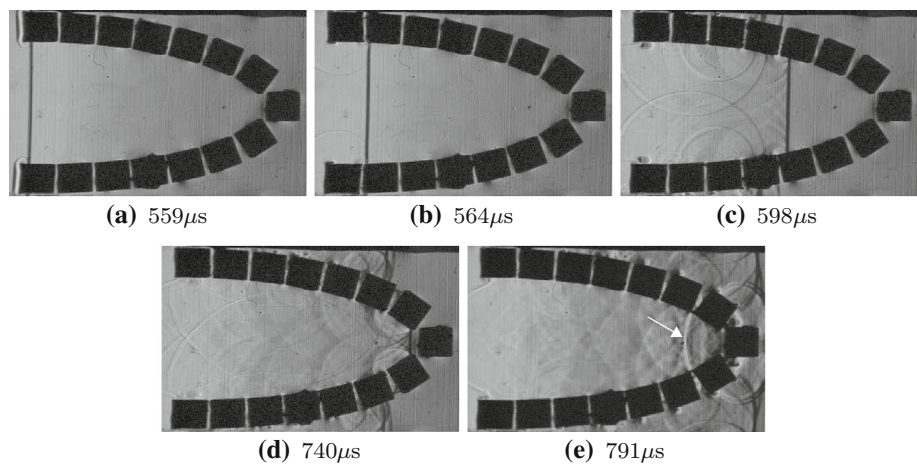
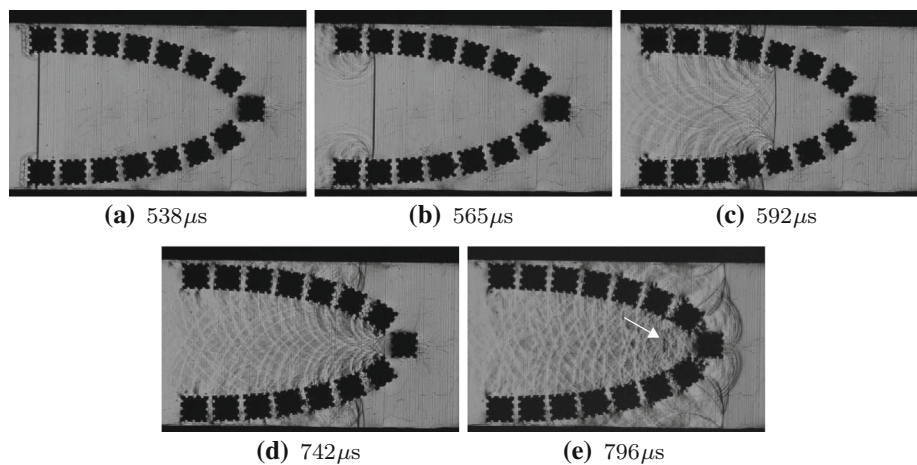


Fig. 10 Experimental schlieren photographs for the case of a logarithmic spiral with three-groove obstacles. Time $t = 0 \mu\text{s}$ corresponds to the time instant when the shock wave passes sensor S_1 . The arrow in frame (e) shows the location of the reflected shock wave. Frame rate: 333,333 frames per second



reduced to the size of a single obstacle, as shown in Figs. 9d and 10d. This is observed for both the zero- and three-groove logarithmic spirals. Once the incident planar shock wave impacts the center obstacle, a main reflected shock wave is created. The reflected shock wave can be seen in Figs. 9e and

10e and is marked by a white arrow. Due to the abundance of reflected shock waves and disturbances created by the three-groove logarithmic spiral, it is difficult to see the reflected shock wave in a still image, but inspection of all the frames in video format makes its position clear. The transmitted

shock wave in both cases forms downstream, and, therefore, does not appear in the schlieren images. In Figs. 9e and 10e, vortices have formed on the outside edge of the obstacles.

The main difference between the two configurations is that the three-groove spiral produced more reflected shock waves. These shock waves and disturbances can be seen throughout all the photographs where the incident shock wave was propagating through the three-groove spiral. Due to these observations, it was hypothesized that the three-groove obstacles would be more successful in mitigating the transmitted and reflected shock waves momentum.

4.5 Logarithmic spiral pressure analysis

Of the three pressure sensors that are incorporated into the shock tube, the results will focus on the data from the most upstream and the most downstream sensors, i.e., sensors S_1 and S_3 . These pressure sensors were chosen, because they provide insight on how the reflected and transmitted shock waves react after having passed through the logarithmic spiral. Sensor S_1 is able to capture data regarding the reflected shock wave, while sensor S_3 provides insight on the transmitted shock wave. When evaluating the peak pressure obtained by the zero- and three-groove logarithmic spirals, it is clear that the greatest pressure was measured by sensor S_1 . The maximum pressure is caused by the reflected shock waves coalescing into a reflected planar shock wave, resulting in a significant increase in pressure.

A comparison of the average pressure measurements for the zero- and three-groove cases is shown in Fig. 11. Results show that, on average, sensor S_1 experiences a slightly lower pressure for the three-groove logarithmic spiral case than for the zero-groove case. This finding is supported by data listed in Tables 1 and 2, where the average peak pressure experienced by sensor S_1 is slightly lower for the three-groove case. As observed from the schlieren photographs, the three-groove spiral produces more reflected shock waves than the zero-groove spiral, which should reduce the energy and the momentum from the incident shock wave. When the incident shock wave collides with the center obstacle, more momentum is lost. After the collision, a reflected shock wave

forms and must travel through the turbulent environment that the three-groove logarithmic spiral created. Traveling through this turbulent environment, which includes vortices and smaller reflected shock waves, further takes away from the momentum of the reflected shock wave. After the five experiments were conducted for both the zero and three-groove logarithmic spirals, and the results were averaged, the three-groove spiral case was able to achieve a lower peak pressure measured by sensor S_1 by 3.91 kPa. This result is attributed to the more turbulent environment that the three-groove logarithmic spiral produced.

The three-groove spiral was able to better mitigate the reflected shock wave, but the results for the transmitted shock wave are less definitive. Figure 12 shows the comparison of pressure impulse between the sensors. Results show that the three-groove spiral on average recorded higher pressure readings for sensor S_2 . This is further supported by the results from sensor S_2 from both zero- and three-groove logarithmic spirals summarized in Tables 1 and 2. The three-groove spiral, on average, produces a peak pressure 2.944 kPa higher than its zero-groove counterpart. The opposite is true when looking at S_3 recordings. The three-groove spiral on average produces 3.813 kPa lower peak pressure than the zero-groove spiral. Peak pressure data only tell part of the story, and thus, pressure-impulse data were used to further investigate shock wave mitigation.

The pressure impulse represents the overall effect which the pressure has on the momentum of the shock wave over the duration of that experiment. The plots in Fig. 12 demonstrate how the pressure impulse develops over time, and results are summarized in Tables 3 and 4. The pressure impulse was calculated over the same time interval for each respective pressure sensor. Therefore, the time intervals from each sensor from the ten total experiments were recorded. Out of ten total experiments, the minimum time each sensor recorded was used to integrate over the pressure. An equal time interval for every sensor allows numerical and visual comparison between the pressure impulse from the different experiments to be possible.

Sensor S_1 experienced 1.7813 kPa \times ms less pressure impulse with the three-groove logarithmic spiral. This fur-

Fig. 11 (Color online) Average pressure for the three sensors S_1 , S_2 , and S_3 for both the zero-groove case (solid lines in color) and the three-groove case (dashed lines in black)

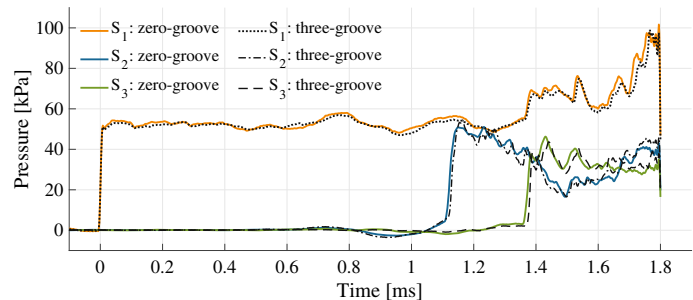


Fig. 12 (Color online) Average pressure impulse for sensors S_1 to S_3 for both the zero-groove (solid lines in color) and the three-groove case (dashed lines in black)

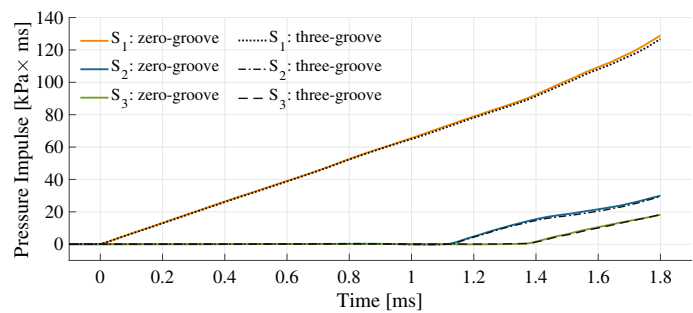


Table 3 Pressure impulse for zero-groove logarithmic spiral with data normalized by an empty test section result in parenthesis

	Pressure impulse [kPa × ms]		
	Sensor S_1	Sensor S_2	Sensor S_3
Experiment 1	99.13 (1.12)	22.71 (0.67)	13.53 (0.61)
Experiment 2	102.12 (1.16)	23.55 (0.69)	13.90 (0.63)
Experiment 3	105.46 (1.20)	24.34 (0.71)	14.53 (0.66)
Experiment 4	107.59 (1.22)	25.09 (0.74)	15.01 (0.68)
Experiment 5	100.95 (1.15)	23.75 (0.70)	13.93 (0.63)
Average	103.01 (1.17)	23.89 (0.70)	14.18 (0.64)
Std. Dev.	3.46	0.89	0.59

Table 4 Pressure impulse for three-groove logarithmic spiral with data normalized by an empty test section result in parenthesis

	Pressure impulse [kPa × ms]		
	Sensor S_1	Sensor S_2	Sensor S_3
Experiment 1	99.10 (1.12)	23.40 (0.69)	14.07 (0.64)
Experiment 2	98.80 (1.12)	23.07 (0.68)	13.82 (0.63)
Experiment 3	106.99 (1.21)	24.61 (0.72)	15.06 (0.68)
Experiment 4	102.00 (1.16)	23.62 (0.69)	14.20 (0.64)
Experiment 5	99.25 (1.13)	22.99 (0.68)	14.08 (0.64)
Average	101.23 (1.15)	23.54 (0.69)	14.25 (0.65)
Std. Dev.	3.47	0.65	0.48

ther supports the evidence previously presented that the three-groove logarithmic spiral more effectively mitigates the reflected shock waves. When comparing the pressure impulse experienced by sensors S_2 and S_3 , the numerical and visual results show that both zero- and three-groove logarithmic spirals were equally effective at mitigating the transmitted shock wave. Sensor S_2 experienced $0.3513 \text{ kPa} \times \text{ms}$ more pressure impulse when the zero-groove logarithmic spiral, while sensor S_3 experienced on average an increase of $0.0701 \text{ kPa} \times \text{ms}$ when using the three-groove logarithmic spiral. However, the difference in pressure impulse measured by sensors S_2 and S_3 is too small to conclude which logarithmic spiral is more effective at mitigating the transmitted shock wave.

After considering both attenuation factors, results indicate that the three-groove logarithmic spiral outperforms the zero-groove logarithmic spiral when attenuating the reflected shock wave, but fails to significantly improve on the mitigation of the transmitted shock wave.

5 Summary

This series of experiments and simulations has been used to study the ability of various logarithmic spiral configurations to mitigate shock waves in a controlled environment. The experiments analyzed the effectiveness of two different configurations of logarithmic spirals: a zero-groove spiral and a three-groove spiral. Although the schlieren photographs illustrate a clear difference in shock dynamics behavior for the two cases, the pressure sensor data do not capture a significant difference between the two cases. The reflected shock wave was less in the case of the three-groove setup with sensor S_1 showing $1.78 \text{ kPa} \times \text{ms}$ less pressure impulse than for the case of the zero-groove case. This is also supported by the peak pressure recording where the average peak pressure experienced by sensor S_1 is slightly lower for the three-groove case (99.27 kPa compared to 101.67 kPa). However, these results are still within the standard deviation resulting from five repeated experiments. One could hypothesize that the small change in cross-section area of 10% of the obstacles containing grooves is not large enough to create a clear difference in pressure signals.

Going forward, different methods will be implemented to better capture and analyze data regarding the transmitted shock waves while investigating the other types of vorticity generating obstacles in addition to those studied earlier by Wan and Eliasson (2015).

Acknowledgements We thank Mr N. Amen for participating in useful discussions with our undergraduate student researchers. We gratefully acknowledge Mr Heng Liu for his assistance with the numerical simulations.

Compliance with ethical standards

Conflict of interest On behalf of all authors, the corresponding author states that there is no conflict of interest.

References

- Andreopoulos Y, Zanthos S, Subramanian K (2007) Moving shocks through metallic grids: their interaction and potential for blast wave mitigation. *Shock Waves* 16:455–466
- Berger S, Sadot O, Ben-Dor G (2010) Experimental investigation on the shock-wave load attenuation by geometrical means. *Shock Waves* 20:29–40
- Berger S, Ben-Dor G, Sadot O (2015) Experimental and numerical investigations of shock-wave attenuation by geometrical means: a single barrier configuration. *Euro J Mech B/Fluids* 50:60–70
- Britan A, Igra O, Ben-Dor G, Shapiro H (2006) Shock wave attenuation by grids and orifice plates. *Shock Waves* 16:1–15
- Chaudhuri A, Hadjadj A, Sadot O, Ben-Dor G (2013) Numerical study of shock-wave mitigation through matrices of solid obstacles. *Shock Waves* 23:91–101
- Henshaw W, Schwendeman D (2003) An adaptive numerical scheme for high-speed reactive flow on overlapping grids. *J Comput Phys* 191:420–447
- Henshaw W, Schwendeman D (2006) Moving overlapping grids with adaptive mesh refinement for high-speed reactive and non-reactive flow. *J Comput Phys* 216:774–779
- Igra O, Wu X, Falcowitz J, Meguro T, Takayama K, Eilig W (2001) Experimental and theoretical study of shock wave propagation through double-bend ducts. *J Fluid Mech* 437:255–282
- Igra O, Falcowitz J, Houas L, Jourdan G (2013) Review of methods to attenuate shock/blast waves. *Prog Aerosp Sci* 58:1–35
- Milton B, Archer R (1969) Generation of implosions by area change in a shock tube. *AIAA J* 7:779–780
- Seeraj S, Skews B (2009) Dual-element directional shock wave attenuators. *Exp Therm Fluid Sci* 33:503–516
- Shi H, Yamamura K (2004) The interaction between shock waves and solid spheres arrays in a shock tube. *Acta Mech Sin* 20:219–227
- Wan Q, Eliasson V (2015) Numerical study of shock wave attenuation in two-dimensional ducts using solid obstacles—how to utilize shock focusing techniques to attenuate shock waves. *Aerospace* 2:203–221

Publisher's Note Springer Nature remains neutral with regard to jurisdictional claims in published maps and institutional affiliations.